ENCLOSURE 2

MFN 13-008

Application of NSF to GNF Fuel Channel Designs, NEDO-33798

Non-Proprietary Information – Class I (Public)

IMPORTANT NOTICE

This is a non-proprietary version of NEDE-33798P, which has the proprietary information removed. Portions of the document that have been removed are indicated by white space with an open and closed bracket as shown here [[ ]].

Global Nuclear Fuel

A Joint Venture of GE,Toshiba, & Hitachi

Global Nuclear Fuel

NEDO-33798
Revision 0
DRF Section 0000-0156-1567 R2
February 2013

Non-Proprietary Information - Class I (Public)

Licensing Topical Report

APPLICATION OF NSF TO GNF FUEL CHANNEL DESIGNS

INFORMATION NOTICE

This is a non-proprietary version of the document NEDC-33798P, Revision 0, which has the proprietary information removed. Portions of the document that have been removed are indicated by an open and closed bracket as shown here [[ ]].

IMPORTANT NOTICE REGARDING CONTENTS OF THIS REPORT

PLEASE READ CAREFULLY

The information contained in this document is furnished for the purpose of obtaining NRC approval of the Licensing Topical Report, *Application of NSF to GNF Fuel Channel Designs*. The only undertakings of Global Nuclear Fuel – Americas, LLC (GNF) with respect to information in this document are contained in contracts between GNF and participating utilities, and nothing contained in this document shall be construed as changing those contracts. The use of this information by anyone other than that for which it is intended is not authorized; and with respect to any unauthorized use, GNF makes no representation or warranty, and assumes no liability as to the completeness, accuracy, or usefulness of the information contained in this document.

TABLE OF CONTENTS

Page

LIST OF TABLES

LIST OF FIGURES

Figure **Title** **Page**

ACRONYMS AND ABBREVIATIONS

Term	Definition
ASTM	American Society for Testing and Materials
BCC	Body Centered Cubic
BOWAVE	Core-Average, Cell-Average Bow used in CPR Methodology
BWR	Boiling Water Reactor
CACABO	Core-Average, Cell-Average Bow calculated in 3D core simulator
CPR	Critical Power Ratio
ECBE	Effective Control Blade Exposure
EPRI	Electric Power Research Institute
GNF	Global Nuclear Fuel
HCP	Hexagonal Close-Packed
HPUF	Hydrogen Pickup Fraction
ISTC	International Science and Technology Center
KAPL	Knolls Atomic Power Laboratory
LHGR	Linear Heat Generation Rate
LOCA	Loss-of-Coolant Accident
LTR	Licensing Topical Report
LWR	Light Water Reactor
MFLCPR	Maximum Fraction of Limiting Critical Power Ratio
NRC	Nuclear Regulatory Commission
NSF	Zr-Sn-Nb-Fe Alloy
R-Factor	Weighted rod local power peaking for critical power calculations
SLMCPR	Safety Limit Minimum Critical Power Ratio
SPP	Second Phase Particles
TEM	Transmission Electron Microscopy
TMOL	Thermal-Mechanical Operating Limit
UTS	Ultimate Tensile Strength

EXECUTIVE SUMMARY

The purpose of this licensing topical report (LTR) is to request approval to use NSF, a fully recrystallized Zr-Sn-Nb-Fe alloy, for channel components within Global Nuclear Fuel (GNF) fuel assemblies used in boiling water reactors (BWRs). The material properties of NSF that are necessary to support licensing of channels are provided in Section 2. [[

]]

In addition to providing the material properties that are used to ensure NSF channels meet all design requirements, GNF is requesting Nuclear Regulatory Commission (NRC) approval of a minor modification of the core-average, cell-average bow input to the channel-bow dependent critical power ratio (CPR) calculations. The bow inputs are currently based on performance of Zircaloy channels and need updating because of the improved channel bow characteristics of NSF channels compared to Zircaloy channels. The CPR methodology is described for information in Section 3; this section includes a description of how the core-average, cell-average bow is calculated and how it is applied in the R-factor methodology to account for channel bow in the CPR calculation. [[

]] Thus, GNF is recommending that once a plant has transitioned to NSF channels, the core-average, cell-average bow will be [[

]].

1.0 INTRODUCTION

The purpose of this licensing topical report (LTR) is to request approval to use NSF, a Zr-Sn-Nb-Fe alloy, for channel components within Global Nuclear Fuel (GNF) fuel assemblies used in boiling water reactors (BWRs). NSF will be discussed in terms of the performance requirements, described in References 1 and 2, for BWR fuel channels. In addition, an evaluation of how NSF will affect the calculation of the critical power ratio (CPR) and the linear heat generation rate (LHGR) is included. Because the GNF methodology for CPR has a channel-bow dependence, GNF is also requesting NRC approval of a minor modification to the bow assessment and application approach for use with NSF channels.

A schematic of a typical BWR fuel assembly is shown in Figure 1-1. It consists of a fuel channel placed over a fuel bundle that contains an array of ~100 fuel rods, one or more water rods, spacers distributed axially, and an upper and lower tie plate. BWR fuel assemblies are placed within a control cell that consists of four fuel assemblies in a square array defined by the top guide structure (see Figure 1-2). A cruciform-shaped control blade moves between the fuel assemblies to control reactivity.

The fuel channel under normal operating conditions (1) provides a guide for control blade insertion, (2) directs reactor coolant flow over the fuel rods effectively defining the flow envelope, and (3) controls the coolant flow leakage at the channel/lower tie plate interface. In addition, for transients and accident conditions, the channel (1) provides the structural stiffness for the fuel bundle to withstand fuel drop and seismic/loss-of-coolant accident (LOCA) loads and (2) transmits fuel assembly seismic loads to the top guide and fuel support. To perform these functions the channel must:

1. Maintain shape – avoid excessive channel distortion
2. Maintain structural integrity – avoid failure; avoid excessive metal thinning from corrosion

To ensure that channels perform their functions, evaluations that depend on the material properties are completed during the design phase. These evaluations are listed in Table 1-1 with reference to the governing licensing topical report and the material properties used in the evaluations. The NSF material properties documented in Section 2 are used to confirm fuel channel design adequacy as defined in References 1 and 2. The effect of NSF channels on CPR and LHGR calculations is provided in Section 3.

Table 1-1 Material Properties for Designing Channels

Design Evaluation	Governing LTR	Material Properties
[[		
		]]

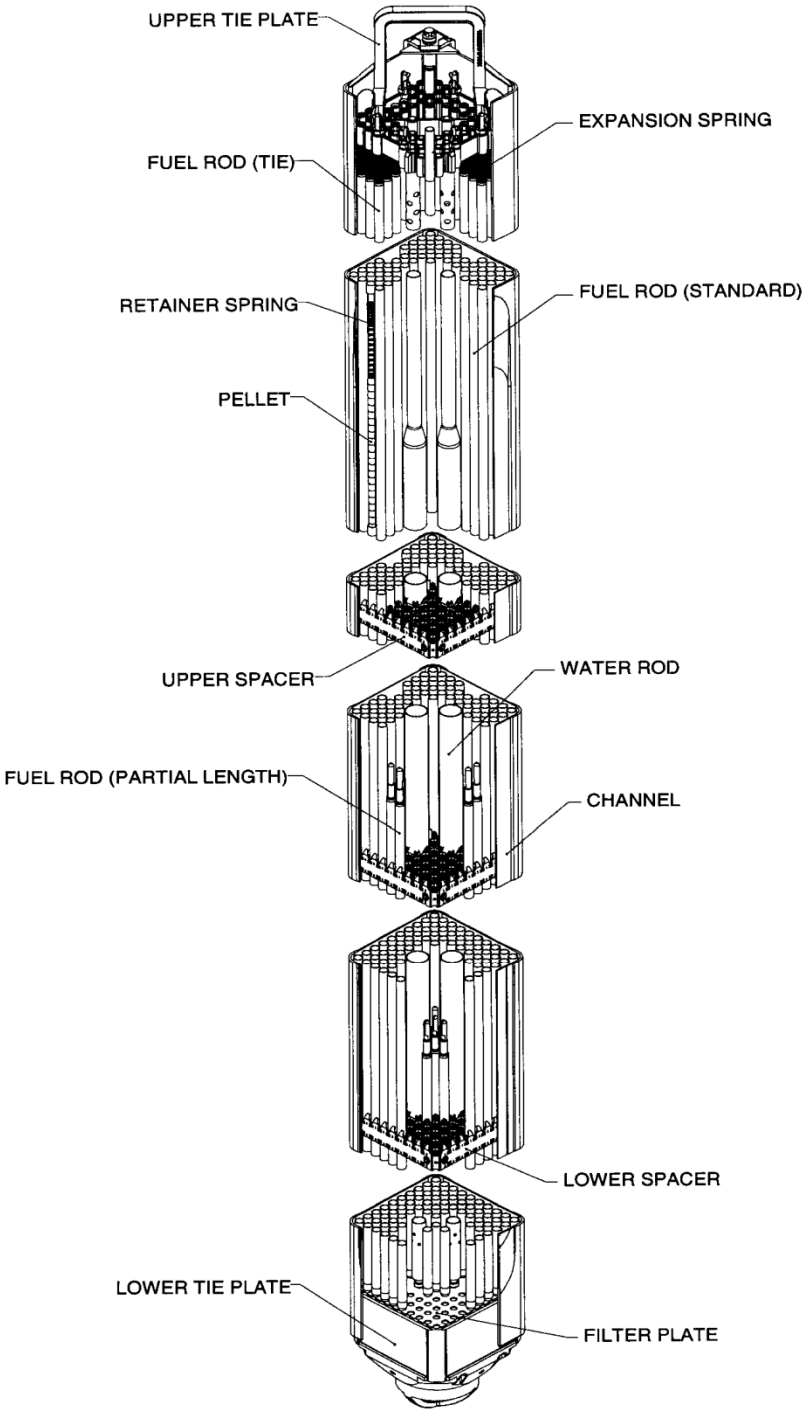

Figure 1-1 Schematic of a Typical BWR Fuel Bundle Assembly

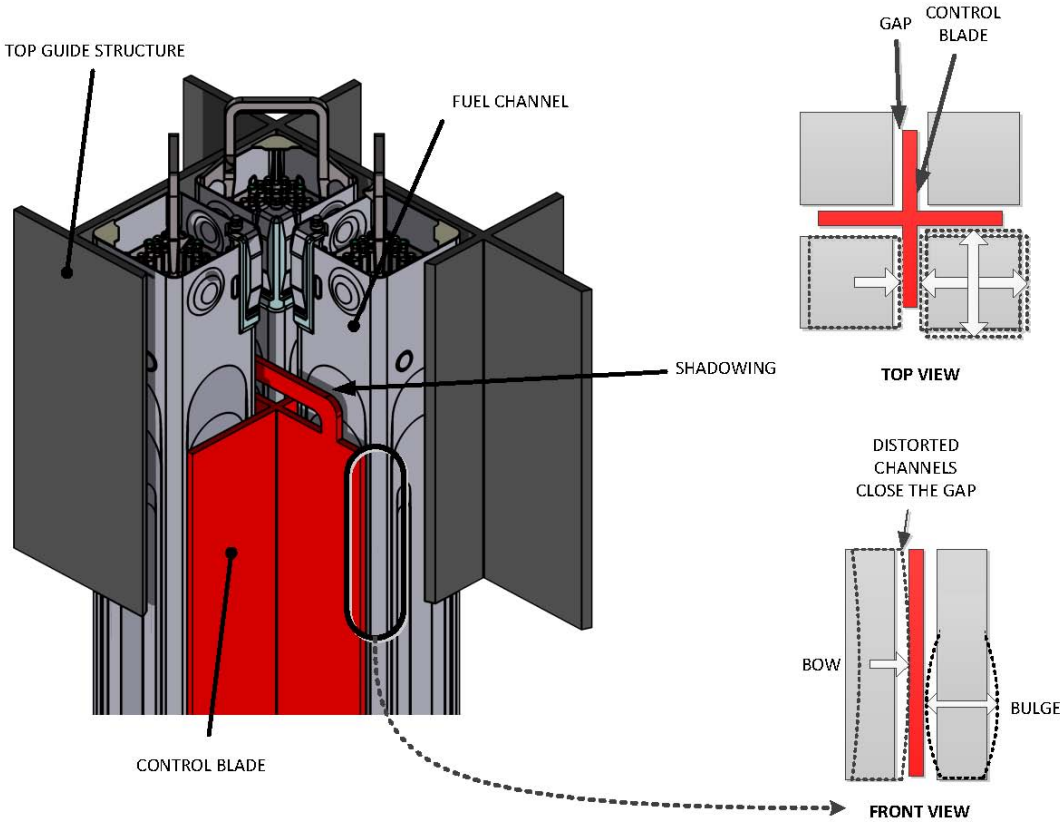

Figure 1-2 Schematic of a BWR Control Cell

Figure Note: The figure also shows the relative distortion caused by channel bow and bulge. Channel bow is generally greatest at the center elevation while bulge is larger near the bottom of the core because the pressure drop across the channel wall decreases as the elevation increases.

2.0 NSF MATERIAL MICROSTRUCTURE AND PROPERTIES

2.1 HISTORICAL PERSPECTIVE ON ZR-SN-NB-FE ALLOYS

In 1955, the groundbreaking work on the use of zirconium alloys in light water reactors (LWRs) within Admiral Rickover's Naval Reactors program became public knowledge (References 3 and 4). The work within the Naval Reactors program culminated with the development of the Zircaloy series alloys (Zircaloy-2 and Zircaloy-4). After these publications, work on other zirconium alloys began throughout the world. In 1958 at the 2nd International Conference on the Peaceful Uses of Atomic Energy, the Russian industry published a series of papers on Zr-Nb alloys (References 5 and 6). Soon afterwards the British and Canadians published work on Zr-Nb alloys (References 7 and 8). This work culminated with the development of alloys E110 (Zr-1%Nb) and E125 (Zr-2.5%Nb) that were used in the Russian VVWR and RMBK reactors for cladding and pressure tube applications and the use of Zr-2.5%Nb alloys for pressure tubes in the CANDU reactors.

In the late 1960s and early 1970s, work continued on these Zr-Nb alloys but with the additions of Sn and Fe. While Kass (Reference 9) found little benefit of Nb additions to Zircaloy-4 when considering only out-of-reactor corrosion, Amaev et al. found encouraging corrosion performance in-reactor for an alloy designated E635 (Zr-1%Sn-1%Nb-0.5%Fe, Reference 10). The Amaev work led Sabol and McDonald to re-evaluate the Kass work on Nb additions to Zircaloy-4 (Reference 11). They found out-of-reactor corrosion performance improved with the Nb addition contrary to Kass's conclusion, and this led eventually to the development of ZIRLO™ (Zr-1%Sn-1%Nb-0.1%Fe, References 12-14). Sabol reported that in a PWR environment the in-reactor corrosion rate of ZIRLO™ was ~60% of Zircaloy-4, the irradiation growth rate was ~50% of Zircaloy-4 and the creep rate was ~80% of Zircaloy-4. In addition, the hydrogen pickup characteristics of ZIRLO™ were similar to Zircaloy-4 (Reference 13).

The Russian industry continued to develop knowledge on the performance of E635 and documented its performance benefits in 1996 (Reference 15). By then the composition of E635 had changed slightly from the 1970 version to have higher Sn and lower Fe with the Fe now being more similar to NSF (see Table 2-1 in Section 2.2). Nikulina et al. reported similar results for E635 as Sabol did for ZIRLO™. Autoclave corrosion performance of E635 was better than Zircaloy-4 in 360°C water and significantly better in 500°C steam but slightly worse in 400°C steam. In-reactor corrosion of E635 under both the boiling RBMK conditions and the non-boiling VVER conditions was comparable to what is typically observed for Zircaloy-2 and Zircaloy-4 in normal BWR conditions. The out-of-reactor thermal creep rate of E635 was also found to be less than Zircaloy-4 at 385°C. The in-reactor creep rate was also lower but measured at higher temperatures than applicable to BWR conditions. The main performance improvement suggested for E635 was a dramatic decrease in irradiation growth compared to Zircaloy-4 and Zircaloy-2; it was found to be resistant to breakaway growth (see Figure 2-1). Although, the irradiation temperature was higher than typical for BWR conditions, this result supported the use of NSF as a channel material where fluence-gradient induced bow was a concern.

When Nikulina et al. published their work on E635 in 1996, GE had been evaluating the use of Zr-Nb based alloys in BWR conditions for approximately 15 years, and soon after this publication, GE initiated a collaborative project with the Russian industry through International Science and Technology Center (ISTC) Project #597 (Reference 16). The objective of this collaborative work was to evaluate the irradiation growth performance of NSF compared to E635 in the BOR-60 fast reactor in Dimitrovgrad, Russia. The samples were evaluated after reaching a fluence of 11 x 10^{21} n/cm^2 (Reference 17). The samples were reinserted and irradiated in an Electric Power Research Institute (EPRI) program to a fluence of 27.8 x 10^{21} n/cm^2 – approximately twice the end-of-life fluence experienced in a BWR (Reference 18). The results of this irradiation growth test program confirmed that NSF was resistant to the breakaway growth that occurs in Zircaloys. In parallel to this irradiation growth program with the Russian industry, GNF began inserting NSF channels into operating BWRs in 2002. As of November 2012, 35 NSF channels have been inserted into operating BWRs in seven different lead-use-channel programs. Eleven NSF channels have operated to end-of-life conditions. The data from these lead-use-channel programs and the irradiation growth program will be discussed in later sections.

2.2 COMPOSITION AND MICROSTRUCTURE OF NSF

2.2.1 Composition

NSF is a zirconium alloy with additions of niobium, tin and iron. The nominal composition by weight (wt %) is: Zr (base) with 1.0% Nb, 1.0% Sn and 0.35% Fe, and shares similarity with two other alloys in the Zr-Nb-Sn-Fe family with operational experience in LWRs, namely ZIRLO^{TM} and E635 (see Table 2-1).

2.2.2 Zirconium

Zirconium is a metal with a hexagonal close-packed (HCP) crystal structure at room temperature – referred to herein as the α phase (see Figure 2-2). The lattice parameters for zirconium at room temperature are: a = 0.323 nm and c = 0.515 nm where the a-direction lies in the hexagonal close-packed basal plane and the c-direction is perpendicular to the basal plane and parallel to the basal pole (Reference 3). When the temperature increases above 863°C, alpha zirconium goes through an allotropic phase transformation where the crystal structure changes from the α phase to a body centered cubic (BCC) β phase. With further increase in temperature, zirconium melts at 1852°C.

Similar to other HCP metals, the mechanical properties of zirconium and its alloys are dependent on the orientation of the crystal. This becomes important after an operation like rolling where deformation causes the grains in polycrystalline zirconium alloys to become preferentially oriented or textured. A recrystallization anneal after rolling, like that used for NSF, causes a rotation of the lattice around the basal pole but does not affect the basal pole distribution. The texture is characterized by the Kearns factors, which represent the relative fraction of crystallographic poles in the longitudinal (f_L), transverse (f_T) and normal (f_N) orientation. For a

rolled zirconium alloy in the fully recrystallized state, typical Kearns factors for basal poles are [[ ]].

2.2.3 NSF Alloy

When alloying elements are added, they either go into a solid solution or precipitate out as a second phase depending on the concentration and temperature. The alloying elements in NSF, like the Zircaloys, result in a two-phase microstructure. In NSF, the Sn[1], O and portions of Nb[2] will be in solid solution with the α-Zr matrix at operating temperatures (288°C). While the remainder of the Nb and essentially all of the Fe combine with Zr to create small second phase particles (SPPs) that are distributed uniformly within an α grain structure. The SPPs in NSF have been identified to be of the $Zr(Nb,Fe)_2$ type at low and intermediate temperatures.

The specific concentrations of the major alloying elements are controlled during the ingot melting process. The range of alloy composition for NSF is provided in Table 2-2. [[

1 Based on the phase diagram for Zr-Sn, as much as ~5%Sn (~0.04 mole fraction) can be in solution with Zr at ~288°C (Reference 19).

2 Based on the phase diagrams for Zr-Nb, approximately 0.3 wt% Nb is in solution with Zr at the operating temperatures (References 20 and 21).

]]

Thus, it is concluded that the properties of NSF, which control channel performance, are insensitive to the range of alloy content defined in Table 2-2.

2.2.4 Microstructure

The standard microstructure of NSF (except in weld-zones) in channels is a fully recrystallized grain structure with uniform distribution of SPPs. Because the microstructure is developed in the channel strip process, the microstructure will be discussed in terms of that expected for a channel strip. The normal manufacturing process to produce channel strip begins with an ingot that is triple melted for homogeneity. The ingot is then forged, hot rolled, and beta quenched. The beta quench dissolves all of the SPP's into solid solution at temperature to precipitate them into finer, more dispersed particles upon cooling. After beta quenching, the final thickness of the strip is then produced by a sequence of hot and cold rolling to final size with intermediate and final anneals. The cumulative annealing after beta quenching determines the SPP size while the final anneal fully recrystallizes the grain structure.

The current process used to manufacture NSF strip for use in channels was originally developed for Zircaloy-2 and Zircaloy-4 to optimize the SPP size and distribution for improved corrosion resistance in BWR environments. Subsequent processing of the strip into channels has no effect on the microstructure except in the seam welds, which is discussed in Section 2.2.4.3. The corrosion performance of NSF in the fully recrystallized state will be discussed in Section 2.10.

2.2.4.1 Grain Size

Because the strip processing of NSF is based on Zircaloy-2 and Zircaloy-4 technology, the final products are in the recrystallized annealed condition and the average grain size in NSF strip is similar to these alloys. The similarity of Zircaloy-4 (Figure 2-3a) and NSF (Figure 2-3b) is shown below. The grain size is approximately [[ ]] in diameter.

2.2.4.2 Second Phase Particles

The second phase particles in NSF are intermetallics with a composition of $Zr(Nb,Fe)_2$, which can be observed using modern electron microscopy techniques. In Figure 2-4 below, the SPP's are shown as dark, solid circles by transmission electron microscopy.

2.2.4.3 Weld Microstructure

Welding is an important joining process in manufacturing channels. For example, channel boxes are produced from two strips that are bent and seam welded full length along two opposite sides of the square box. Because the metal is melted and rapidly cooled during welding, the microstructure has a Widmanstätten grain structure (see Figure 2-5) rather than an equiaxed grain structure typical of a fully recrystallized material. In addition, the melting and solidification randomizes the texture in the weld zone.

The performance of NSF with the weld microstructure will be discussed as needed in subsequent sections.

2.2.5 Texture

GNF has developed a range of acceptable crystallographic texture values based on many years of performance in-reactor. This acceptable range of texture values serves as a foundation for comparison when changes in alloy elemental concentrations or material processing are made. This ensures control of texture in the manufacturing process, which can often be influenced by processing changes such as hot and cold rolling of strip more than alloy changes. Processing developed for NSF is similar to Zircaloy-2, and texture measurements taken using X-Ray diffraction techniques of the basal crystallographic pole have provided statistically similar results to Zircaloy-2 as shown in Table 2-3.

For material in the weld-zone, the texture is random and the Kearns factors are $f_L = f_T = f_N = 0.33$.

2.3 ELASTIC PROPERTIES

The elastic properties of solids with metallic bonding are directly related to the stiffness of the interatomic bonds. Although ultimately metallic bonding follows quantum mechanics, a simplified spring model representing the interatomic bonds may be used to predict elastic properties. With such a spring model, the elastic modulus is estimated with the following equation (Reference 25):

$$E = \frac{\alpha q^2}{4\pi\varepsilon_o r_o^4} \quad \textbf{(2-1)}$$

Where $\alpha = (n - 1)$ with n being the coordination number (or the number of closest neighbors), q is the charge of the metal ion, ε_o is the permittivity of vacuum, and r_o is the nominal bond length.

In dilute alloys such as Zircaloy-2, Zircaloy-4 and NSF, where zirconium makes up approximately 97.5 % of the alloy, the charge of a zirconium ion and the bond length of the zirconium lattice controls the elastic properties, and the difference between Zircaloy and NSF is insignificant. Thus, it is reasonable to apply the elastic properties (modulus and Poisson's Ratio) of Zircaloy to NSF.

The Young's modulus of these zirconium alloys as a function of temperature and direction is given by:

$$\boldsymbol{E_i = A + BT} \quad \textbf{(2-2)}$$

Where E_i is the Young's modulus in lb/in^2, T is the temperature in $^\circ$F, A and B are constants given in Table 2-4, and i is the direction (1-through-thickness, 2-transverse or 3-rolling).

Similar to the Young's modulus, the Poisson's Ratio (ν_{ij}) is a linear function of temperature such that

$$\boldsymbol{\nu_{ij} = A + BT} \quad \textbf{(2-3)}$$

Where T is temperature in ^{o}F, A and B are constants and i and j are directions. The values of A and B are given in Table 2-5.

2.4 THERMAL EXPANSION

Thermal properties, such as thermal expansion, can be temperature and texture dependent. As discussed in Section 2.2.5, texture for NSF is similar to that for Zircaloys, when manufactured using equivalent process sequences; therefore, no changes in thermal expansion occur due to texture. Thermal expansion properties are not sensitive to small changes in composition, such that Zircaloy-2 and Zircaloy-4 are properly treated without differentiation. However, thermal expansion can be composition dependent if the compositional change is large. [[

]].

In Figure 2-6, the thermal expansion of NSF as a function of temperature is shown together with that for Zircaloy-2. For each alloy, measurements were obtained from channel strip materials along the transverse and longitudinal directions. Both materials were tested in the recrystallized state. The figure also shows the thermal expansion design lines along these directions for recrystallized Zircaloys.

For recrystallized Zircaloys and NSF, the thermal expansion is given by

$$\frac{\Delta i}{i_o}\ (\text{in / in}) = \alpha_i \left(T - 68^\circ F\right) \quad \textbf{(2-4)}$$

where

Gi=change in the i dimension

i_O=i dimension at ambient temperature (68°F)

i=directional index, L, t, or r, where

L=longitudinal (axial) direction,
t=transverse (circumferential) direction
r=radial (normal) direction

h i=coefficient of thermal expansion in the i direction ($°F^{-1}$).

[[ ]]

where

f_i=basal pole texture factor in the i direction,

T=temperature (°F)

The design lines are consistent with that for cladding (Reference 26) but are shown in Figure 2-6 with basal pole texture parameters (see Table 2-3) of [[ ]] appropriate for channel strip along, respectively, the longitudinal and transverse directions. [[

]]

2.5 SPECIFIC HEAT

The specific heat (or heat capacity per unit mass) is the slope of the function between absorbed energy and temperature (i.e., ΔQ/ΔT on a per mass basis); typical units are J/kg-K. The specific heat of a material is mostly a function of the vibrational response of atoms (Reference 27), and when elements are combined the specific heat is modeled as the weighted sum of the constituents (Reference 28):

$$(C_P)_{A_xB_y} = x(C_P)_A + y(C_P)_B \quad \textbf{(2-5)}$$

Where $(C_p)_A$ and $(C_p)_B$ are the specific heats of the constituents and x and y are the mass fractions.

With this relationship the specific heat of Zircaloy-2 and NSF may be assessed. Table 2-6 provides the specific heats of the constituents and the relative mass fractions of Zircaloy-2 and NSF. Using Equation (2-5), the specific heat of Zircaloy-2 is calculated to be 280.0 J/kg-K at 25°C and NSF is calculated to be 280.3 J/kg-K at 25°C. These values are within the expected measurement variability, and thus, the specific heat used by GNF for [[
]].

The GNF model for specific heat of the alpha phase [[ ]] has the standard temperature dependence.

$$\boldsymbol{C_p = A + B(T) + C(T)^{-2}} \text{ (J/kg·K)} \quad \textbf{(2-6)}$$

Where T is the temperature in K and A, B and C are constants with values of [[
]], respectively.

For the temperature range [[ ]], Zircaloy is in the α + β phase regime and the specific heat is given by:

$$\boldsymbol{C_p = A + B(T) + C(T)^{2}} \text{ (J/kg·K)} \quad \textbf{(2-7)}$$

Where [[ ]].

At temperatures greater than 1248.6 K, Zircaloy is in the beta phase and the specific heat is given by

[[ ]] **(2-8)**

2.6 THERMAL CONDUCTIVITY

The thermal conductivity is related to specific heat in the following way (Reference 29):

$$\boldsymbol{k = \rho C_p D_T} \quad \textbf{(2-9)}$$

where ρ is the density, and D_T is the thermal diffusivity, which typically has units of cm^2/s. Given the measured density (Section 2.7) and the specific heat of NSF are equivalent to Zircaloy, any potential difference in thermal conductivity would be related to differences in thermal diffusivity. The thermal diffusivity of NSF was measured and found to be equivalent to Zircaloy-2. A summary of those measurements and the subsequent calculated thermal conductivities are provided in Table 2-7.

The GNF model used for the thermal conductivity of [[ ]]. The form of the model is as follows

$$K = C_1 + C_2T + C_3T^2 + C_4T^3 \quad \textbf{(2-10)}$$

where K is the thermal conductivity in W/m-K, T is the temperature in K, and C_1, C_2, C_3, and C_4 are constants with values, [[ ]], respectively.

Figure 2-7 plotted the data in Table 2-7 as a function of temperature and compared to the model in Equation (2-10) and historical data from a Knolls Atomic Power Laboratory (KAPL) report (Reference 30). The model used by GNF predicts both the historical and current data well.

2.7 DENSITY OF NSF

The density of NSF was measured and found to be [[ ]].

2.8 PLASTIC PROPERTIES

The yield strength and UTS are material properties that represent a material's resistance to plastic deformation and failure by a plastic instability. The yield strength represents the stress where significant plastic deformation begins to occur, and the ultimate strength represents the stress needed to cause a plastic instability leading to failure.

The tensile properties of NSF were measured at [[ ]]in the unirradiated condition and at [[ ]]in the irradiated condition (See Table 2-8). Because the strength of zirconium alloys, like NSF, decreases with increasing temperature and increases with irradiation, channels are designed for the most limiting condition assuming the material is unirradiated and the temperature is 550°F. Effectively, the most limiting condition is when the fuel is fresh and the reactor has just started. [[

]].

These measured plastic tensile properties are used to develop a model for the plastic deformation based on the following relationship:

$$\sigma_T = K(\varepsilon_p)^n(\dot{\varepsilon})^m \quad \textbf{(2-11)}$$

where:

σ_T is the true stress in ksi,

K is the strength coefficient (ksi-s^m),

ε_p is the true plastic strain (in/in),

$\dot{\varepsilon}$ is the strain rate in (in/in-s),

n is the strain hardening exponent (dimensionless),

m is the strain rate sensitivity exponent (dimensionless)

The parameters K, n and m are material, direction, temperature, and fluence dependent parameters.

[[

]]

where ϕ is the fast flux in n/cm^2-s (> 1.0 MeV) and t is time in seconds such that ϕt is fluence in n/cm^2 (> 1.0 MeV).

[[

]]

The parameters in the relations above were determined by fitting the model to measured data[3]. When comparing the model predictions to measured engineering strength values (yield and UTS), the true stress is converted to engineering stress using the standard relationships:

$$\boldsymbol{\sigma_{engr} = \sigma_T/(1 + \varepsilon_{engr})} \quad \textbf{(2-21)}$$

and

$$\boldsymbol{\varepsilon_{engr} = exp(\varepsilon_T) - 1} \quad \textbf{(2-22)}$$

The predicted yield strengths and UTS are compared to the measured values in Figure 2-8. The predicted yield strength is calculated at a plastic strain of [[ ]], and the UTS is predicted for the plastic strains reported in Table 2-8.

2.8.1 The Model for Design

A design value for a material property is generally defined as a backoff from a nominal value. In some cases the backoff is defined in statistical terms. For example, in Reference 1, the yield strength and ultimate tensile strength used in channel design were defined as a 95/95 tolerance limit relative to the available data for unirradiated Zircaloy-4 channels at 550°F. In this case, the standard deviation was likely based on a large amount of test data collected to ensure the purchased material met the specified strength. [[

[3] The relationship for *R, V* and *m* are equivalent to those documented in Reference 26, which provides the plasticity model for Zircaloy-2 and Ziron cladding.

]]

giving

$$\sigma_{design} = K_{design}(\varepsilon_p)^n(\dot{\varepsilon})^m \quad \textbf{(2-24)}$$

At the most limiting conditions [[ ]], the design yield strength is given as [[ ]]. The calculated design yield strengths and UTS are compared to the measured values in Figure 2-9.

In practice, the design strength will be controlled in the specification of the material where it is defined as the minimum allowable strength. Testing of each lot documents the objective evidence that the strength of the material is greater than the design value.

2.8.2 Plastic Properties of Weld Metal

The plastic deformation of weld metal was investigated by hardness testing rather than tensile testing. Typical of zirconium alloys, the hardness of the NSF-to-NSF weld microstructure was found to be greater than the hardness of NSF in the fully recrystallized state (see Table 2-10). The implication of the greater hardness is higher yield strength. Thus, it is conservative to assume the plastic deformation properties of fully recrystallized NSF for NSF with a weld microstructure.

2.9 THERMAL AND IRRADIATION CREEP

Thermal creep is the time-dependent permanent deformation of a material that has an applied stress below the yield strength (which is considered the onset of time-independent deformation). If a component is loaded to a constant strain, creep has the effect of decreasing the applied stress when elastic strain is converted to permanent strain. If the component is loaded to a constant stress, permanent deformation increases over time. In traditional thermal creep, at intermediate stress levels this time-dependent permanent deformation occurs mainly by dislocation motion that results from stress-driven diffusion (a time-dependent process). Typically the strain rates of these dislocation-creep mechanisms are found to be a function of the applied stress to a power ($\dot{\varepsilon} \propto \sigma^n$). At lower stresses, thermal creep may also occur without dislocation motion by diffusion through grains (Nabarro-Herring creep) or around grain boundaries (Coble creep), which changes the shape of the grain – resulting in permanent deformation. The strain rates of

these mechanisms are linearly proportional to stress ($\dot{\varepsilon} \propto \sigma$). At high stress, creep transitions to plasticity where the mechanism is stress-driven motion of dislocations that is time-independent.

The addition of a neutron flux and the accumulated damage it causes within a nuclear reactor increases the complexity of creep deformation although the general trend in mechanisms is maintained. At high stress, permanent deformation will result from time-independent motion of dislocations, and the response will follow a plasticity model as described in Section 2.8. The strain rates are such that flux does not enhance creep but the damage from the neutron flux (i.e., fluence) retards irradiation creep. At low stresses the creep rates are low enough that flux enhances creep. In addition, the creep rate is approximately linear with stress (though the mechanism is likely a flux-enhanced, stress-induced irradiation growth mechanism and not related to Nabarro-Herring or Coble creep, Reference 31). Irradiation creep at intermediate stress levels is less well understood. The general consensus appears to be that dislocation-creep mechanisms similar to thermal creep are active and the irradiation creep rate is modeled as function of stress raised to a power (Reference 31). However, the effect of flux and fluence is not fully understood. GNF models the strain rates at intermediate stresses such that fluence retards creep. Most analyses for channel components are characterized by low stress, as is discussed below.

2.9.1 Creep of NSF

The thermal creep of NSF or NSF-type alloys at stresses where dislocation creep dominates is lower than Zircaloy (References 15 and 32). Thus in-reactor, at stress levels where deformation is controlled by dislocation motion, the creep of NSF would likely be less than Zircaloy. Data for ZIRLO™ (Reference 14) and a NSF-like alloy (Reference 33) support this conclusion. [[

]].

Creep bulge in channels occurs because of the differential pressure between the inside and outside of the bundle (see schematics in Figure 1-2 and Figure 2-10). The pressure drop is effectively a constant stress on the channel face that induces an elastic bulge that over time results in permanent strain (i.e., creep bulge). [[

]] The stress in the channel that controls the creep bulge may be estimated at the maximum deflection (δ) as

$$\boldsymbol{\sigma = \frac{\Delta P L^2}{4t^2}} \qquad \textbf{(2-25)}$$

Given typical pressure drop [[

]].

2.9.2 GNF Creep Models for NSF

The models used in design to predict NSF creep deformation of channel components follow those used for cladding in the recrystallized state, which are documented in Reference 26. [[

]]

2.10 CORROSION

As with any in-reactor material the first and foremost performance requirement is that the material withstands corrosion to the extent that it maintains structural integrity, and thus, maintains its ability to perform its design requirements. For channels, maintaining structural integrity is the only corrosion performance requirement, which in practice means that the component must maintain a minimum thickness of metal.

The design basis for channel metal thinning due to corrosion takes into consideration the differences in densities for the metal and oxide. The metal loss from corrosion is defined as

$$t_{Loss} = 0.63(2)Z_{tot} \quad \textbf{(2-31)}$$

Where Z_{tot} is the total zirconium oxide thickness in microns for corrosion on one surface, the factor 2 accounts for two-sided corrosion that occurs on channel components, and the factor 0.63 accounts for the density differences between the oxide and the metal. The total oxide thickness is given by the relationship

$$\boldsymbol{Z_{tot} = Z^{th} + Z^{irr}} \quad \textbf{(2-32)}$$

where:

Z^{th} = thermally activated component of the oxidation (temperature dependent), and

Z^{irr} = the irradiation enhanced component of the oxidation (temperature independent).

For corrosion of Zircaloy-2 and Zircaloy-4, the upper bound thermally activated component is given by:

[[ ]]

where *T* is the temperature in degrees Celsius and *t* is the hot core residence time in years. The upper bound irradiation enhanced component at 288°C for corrosion of Zircaloy-2 is given by:

[[ ]]

The variation of the total zirconium oxide thickness, Z_{tot}, with in-reactor operating time for Zircaloy-2 is shown in Figure 2-12. The figure includes recent hot cell oxide data for both Zircaloy-2 and NSF, which indicates significant margin between the measured corrosion and the design value for both alloys. Because of this significant margin, [[
]]

2.10.1 Effect of Pre-Oxidation

[[

]]

2.11 IRRADIATION GROWTH

Irradiation growth is a unique deformation mechanism in the realm of material performance in that growth strain due to neutron irradiation occurs absent an applied stress. Because of this, irradiation growth is also known as stress-free growth. Irradiation growth is mainly attributed to the anisotropic redistribution of irradiation-induced vacancies and interstitials into dislocation loops on preferred crystallographic planes. Because the interstitial loops cause a positive growth strain and collapsed-vacancy loops cause a contraction, the volume change of irradiation growth is essentially zero (Reference 34). Models for predicting irradiation growth strain (ε) are a function of fluence (ϕt), which is a measure of the amount of irradiation-induced vacancies and interstitials, and the Kearns texture factor (*f*), which is the fraction of basal poles in a given direction (*z* - longitudinal, transverse, normal or weld (i.e., beta-quenched)):

$$\boldsymbol{\varepsilon_z = (1 - 3f_z)f(\phi t)f(T)} \qquad \textbf{(2-35)}$$

In this model, f(ϕt) is an empirical function that captures the phenomenological observations that the irradiation growth rate is initially relatively high, then decreases to almost zero and then increases again to a relatively high rate. The initial growth strain occurs when a-type dislocation loops form; these a-type dislocation loops saturate at low fluences (~1 to 1.5 x 10^{21} n/cm^2), which causes the growth rate to decrease to nearly zero; when the fluence reaches the breakaway fluence (~5 - 8 x 10^{21} n/cm^2), c-type dislocations start to form and the growth rate increases (Reference 35). The third term, f(T), is an empirical function that provides a temperature dependence when calculating irradiation growth at temperature other than 288°C. At 288°C, the value of this function is 1.0. Because irradiation growth of channels occurs at 288°C, this temperature dependence is not considered herein.

[[

]]. This model is shown in Figure 2-13 compared to growth data for Zircaloy-2. Actual growth measurements from irradiated Zircaloy-2 channels are also shown. The channel growth data is consistent with the observation of breakaway growth.

In contrast to Zircaloy, [[

]].

Recently, EPRI has reported irradiation growth from a series of alloys supporting the conclusion that [[

]] These observations were consistent with those reported by Shishov et al. (Reference 22), who found a similar correlation of resistance to irradiation growth and less frequent c-type dislocations for Zr-Nb-Sn-Fe alloys containing a range of Fe (0.35 – 0.65%) and a range of Nb (0.7 – 2.0%).

2.12 FATIGUE

The fatigue behavior of Zircaloy is well characterized in References 37 and 38 (see Figure 2-16), and was previously described to, and approved by, the NRC in Reference 26. The relationship used to describe the data follows the relationship $\varepsilon = bN^k$; where two relationships are used, one for low cycle and one for high cycle fatigue failure. The total (elastic plus plastic) strain amplitude, ε, for a cyclic loading life of N cycles for Zircaloy is as follows:

[[

]]

To evaluate the fatigue performance of NSF, an hourglass shaped fatigue specimen that GNF developed for sheet material in the 1980's was utilized. For comparison purposes, the fatigue testing included both unirradiated and irradiated NSF and Zircaloy-2 channel materials. The irradiated channel coupons were [[

]]

2.13 STRESS RUPTURE

Stress rupture characterizes the time to creep failure due to an applied load on a component. For channels, the differential pressure across the channel wall induces a "hoop" stress in the channel face (see Figure 2-10). Thermal and irradiation creep under the induced stresses result in channel face distortion or channel bulge. GNF design criteria for channels include the long term cumulative effect of creep considering a conservative estimate of time at an applied stress over the operating life history of the channel.

The relationship between applied stress, temperature, fluence and time to failure shown in Equation (2-40) is derived from open literature data as well as GNF test data and is considered conservative when true stress levels remain below 90% of the ultimate strength of the material. To validate NSF performance relative to other Zircaloys, testing was performed on channel material in the irradiated and unirradiated conditions at temperatures consistent with normal operations (288°C) and transient temperatures (400°C). [[

]] The test applies a static load and constant temperature to the test specimen until stress rupture was reached, determining the time to failure due to stress rupture.

Equation (2-40) below, provided in Reference 1 has been used to conservatively predict time to failure for Zircaloy channels. This predictive equation utilizes a Larson-Miller parameter approach to determine the relationship between applied stress, temperature and fluence and time to failure.

[[

]]

The creep performance of NSF and similarly processed Zircaloy has been discussed previously where testing indicates unirradiated NSF has a slightly higher strength than unirradiated Zircaloy-2. [[

]] The data also show that both alloys are conservatively bound by Equation (2-40). Similarly, testing on irradiated Zircaloy-2 and NSF, shown in Figure 2-19, at different temperatures and fluences demonstrates Equation (2-40) conservatively predicts time to failure for either alloy. [[

]].

2.14 HYDROGEN EFFECTS

Corrosion is the major source of hydrogen absorbed by zirconium alloys. At certain levels, this absorbed hydrogen may degrade mechanical properties. The level of hydrogen absorbed (measured in wppm) is directly proportional to the corrosion thickness (Z_{tot}) and the hydrogen pickup fraction (HPUF) while inversely proportional to the thickness of the component (t_m).

The hydrogen pickup in an NSF channel was measured and compared to a Zircaloy-2 channel that operated in symmetric locations throughout life (see Figure 2-20). The measured hydrogen (absorbed) in wppm is plotted relative to the hydrogen generated from corrosion in wppm using the metal as the mass basis for the normalization. [[

]].

The concern with absorbed hydrogen in zirconium alloys is the potential detrimental effect on mechanical properties. In this respect, NSF is expected to be similar to other zirconium alloys. Hydrogen may detrimentally affect mechanical properties when the hydrogen concentration increases above the solubility limit and hydrides form. However, hydride embrittlement depends on the temperature (Reference 20) and on whether failure is caused by a plastic instability or by crack propagation; there is less of an effect on failure by a plastic instability than crack

propagation (References 39 and 40). Yunchang and Koss (Reference 39) investigated the microstructural effects of hydrides on failure by a plastic instability. They found that hydrides promote ductile void growth and coalescence but have little effect on the onset of void formation, which occurs after the instability at the UTS. Similarly, Kuroda et al. (Reference 40) found the burst pressure in a fuel rod was independent of hydrogen (up to 461 wppm) when the hydrides were uniformly distributed and oriented perpendicular to the radial direction (or perpendicular to the through-thickness direction as is the case in a channel component – see Figure 2-21).

Hydrides do potentially have a larger effect when failure is caused by crack propagation. In this case, a propagating crack will seek the path of least resistance. As zirconium hydrides are generally more brittle than the Zr matrix (especially at temperatures below 100°C, Reference 20), a propagating crack will tend to jump from hydride to hydride. The result is that the effective toughness of a zirconium alloy with hydrides may decrease with increasing hydrogen (Reference 20). This is mainly an issue when the hydrides are oriented parallel to the failure plane, which is not the case in channels where the hydrides are oriented perpendicular to failure in the through-thickness direction.

2.14.1 Hydrogen Considerations in Design of NSF Components

[[

]].

2.15 NUCLEAR PROPERTIES

The nuclear properties of NSF have been assessed. The affect can be described as an effect on the infinite lattice eigenvalue determined by lattice physics calculations due to the differences in alloy isotopic content. The difference in infinite lattice eigenvalue between Zircaloy-4 and NSF was found to be of order [[

]]

Table 2-1 Nominal Chemical Weight Percent Composition of Zr-Nb-Sn-Fe Alloys

	NSF	ZIRLO™	E635 Circa 1970	E635 Circa 1996
Nb	1.0	1.0	1.0	1.0
Sn	1.0	1.0	1.0	1.25
Fe	0.35	0.1	0.5	0.37
O	0.12	0.14	0.04	0.06

Table 2-2 Composition Range for NSF

	Composition Range
Nb	[[
Sn	
Fe	
O	]]

Table 2-3 Comparison of Typical Texture Values for NSF Compared to Zircaloy-2

Alloy/Sample	f_N	f_L	f_T	Total f
Zircaloy–2/Typical	[[			
NSF/Typical				]]

Note: This is a comparison of Typical Texture Values for NSF Compared to Zircaloy-2 where f_N, f_L, and f_T are the relative fraction of basal poles in the normal, longitudinal and transverse directions.

Table 2-4 Constants A and B for calculating the Young's Modulus for Zircaloy-2, Zircaloy-4 and NSF

Young's Modulus	A	B
E_1	[[	
E_2		
E_3		
E_β		]]

Note: 1 = through-thickness direction,
2 = transverse direction,
3 = longitudinal direction, and
β = weld metal or Beta-Quenched

Table 2-5 Constants A and B for Calculating the Poisson's Ratio for Zircaloy-2, Zircaloy-4 and NSF

Poisson's Ratio	A	B
ν_{12}	[[	
ν_{13}		
ν_{21}		
ν_{23}		
ν_{31}		
ν_{32}		
ν_β		]]

Note: 1 = through-thickness direction,
2 = transverse direction,
3 = longitudinal direction, and
β = weld metal or Beta-Quenched

Table 2-6 Specific Heat of the Constituent Elements in Zircaloy-2 and NSF (Reference 41)

Element	Specific Heat at 25°C cal/g-K	Specific Heat at 25°C J/kg-K	Zircaloy-2 Mass Fraction	NSF Mass Fraction
Zr	0.067	280.5	.9818	.9765
Nb	0.064	268.0	-	.01
Sn	0.051	213.5	.015	.01
Fe	0.106	443.8	.0015	.0035
Ni	0.106	443.8	.0007	-
Cr	0.107	448.0	.001	-

Table 2-7 Measured Thermal Diffusivity and Calculated Thermal Conductivity of Zircaloy-2 and NSF

Material	Temp (°C)	Measured Thermal Diffusivity (cm^2/s)	Density (g/cm^3)	Heat Capacity (J/kg-°K)	Calculated Thermal Conductivity (W/m-°K)
Zr-2	23	[[			
Zr-2	100				
Zr-2	175				
Zr-2	250				
NSF	23				
NSF	100				
NSF	175				
NSF	250				]]

Table 2-8 Average Measured Yield and Ultimate Strength of NSF Channel Material in the Unirradiated and Irradiated (~9.5 x 10^{21} n/cm^2) Condition

Irradiation Condition	Orientation	Strain Rate (1/min)	Test Temp. (°F)	0.2% offset YS (ksi)	UTS (ksi)	Uniform Elongation (%)	
						Elastic +Plastic	Plastic Only
[[							]]

[[

]]

Table 2-9 Design Yield and Ultimate Strength of NSF Channel Material ([[ ]]in/in/min)

	[[			]]
Yield Strength (ksi)				
UTS (ksi)				

Table 2-10 Rockwell B Hardness Measurements NSF-to-NSF Weld Compared to NSF in the Fully Recrystallized State

Microstructure	Hardness (Rockwell B)
Weld	[[
Weld	
Weld	
Recrystallized	
Recrystallized	
Recrystallized	]]

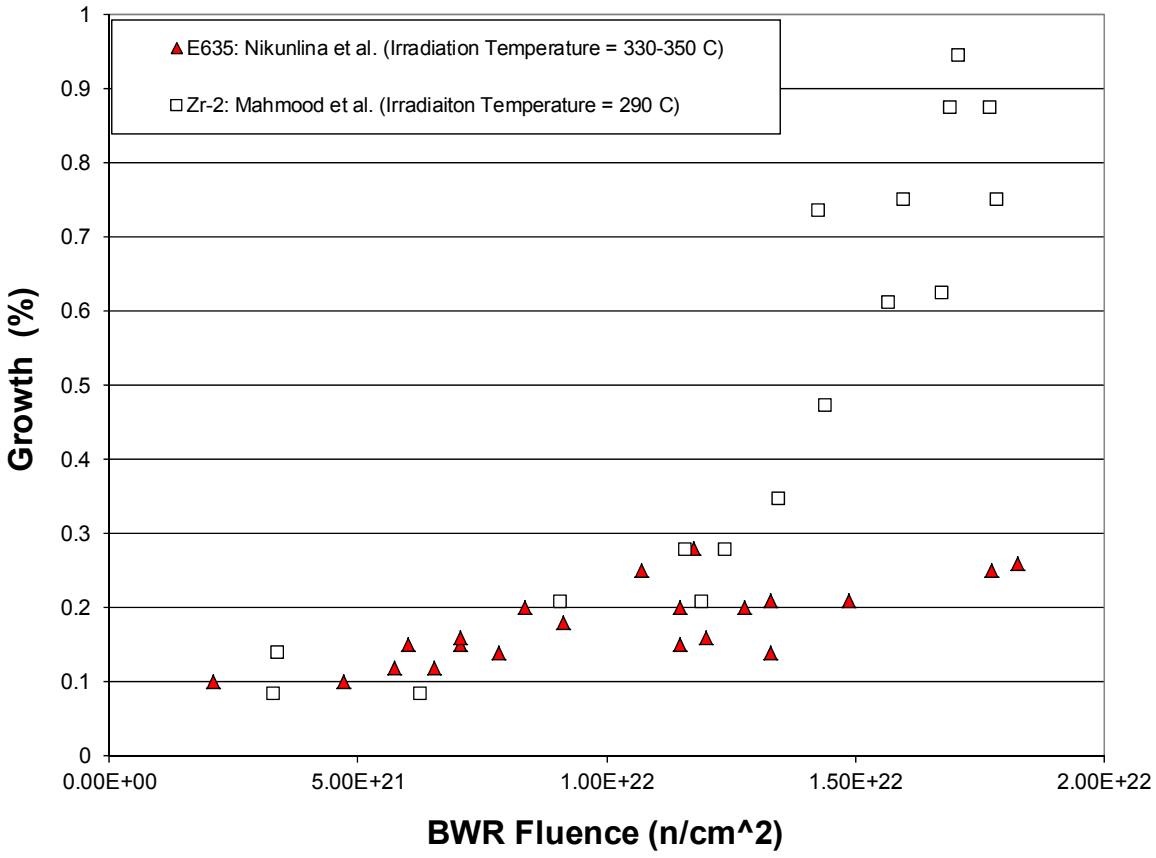

Figure 2-1 Irradiation Growth of E635 (Reference 15) Compared to Zircaloy-2 (Reference 42)

Figure Note: In each case the fast fluence was converted to dpa and then BWR fluence assuming a 40% average void fraction. The conversion factors are provided in Reference 43.

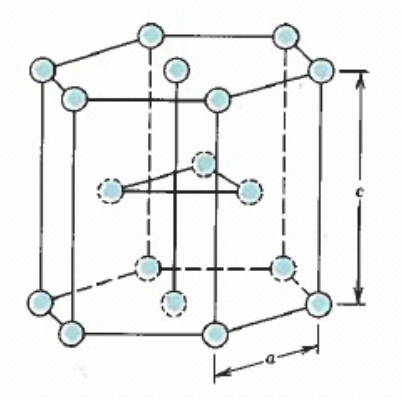

Figure 2-2 Hexagonal Close-Packed (HCP) Crystal Structure of Zirconium

[[

]]

(a) Zircaloy-4 at 548x

[[

]]

(b) NSF at 500x

Figure 2-3 Recrystallized Grain Structure

[[

]]

Figure 2-4 TEM Image of NSF Second Phase Particles

[[

]]

Figure 2-5 Widmanstätten Microstructure of a NSF-to-NSF Weld

[[

]]

Figure 2-6 Thermal Expansion ($dL/L=\Delta i/i_o$) of NSF and Zircaloy-2

Figure Note: Thermal expansion ($dL/L=\Delta i/i_o$) of NSF and Zircaloy-2 obtained on channel strip materials in the transverse (Trans) and longitudinal (Long) directions.

[[

]]

Figure 2-7 Thermal Conductivity of NSF

Figure Note: The thermal conductivity of NSF is compared to the thermal conductivity of Zircaloy-2, the calculated thermal conductivity (Equation (2-10) and historical data on Zircaloy (Reference 30). The uncertainty on the GNF thermal conductivity data is shown as **[[ ]]**.

[[

]]

Figure 2-8 Measured Strength of NSF (yield and UTS) Compared to the Predicted Strength Using the NSF Plasticity Model

[[

]]

Figure 2-9 Measured Strength of NSF (yield and UTS) Compared to the Design Strength Using the NSF Plasticity Model

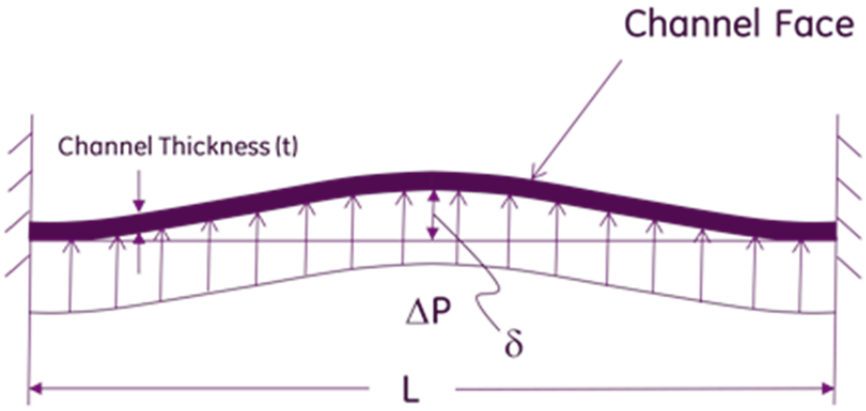

Figure 2-10 Schematic of Force and Deflection on a Channel Face

[[

]]

Figure 2-11 Creep Bulge Measurement for NSF and Zircaloy-2 Channels taken at the 40 in. Elevation

Figure Note: Creep bulge measurement for NSF and Zircaloy-2 channels taken at the 40 inch elevation, where typically the bulge is a maximum.

[[

]]

Figure 2-12 Upper bound Design Value for Corrosion and Recent Hot Cell Oxide Thickness Data for Zircaloy-2 and NSF

Figure Note: Uncertainty bars represent one standard deviation.

[[

]]

Figure 2-13 GNF Channel Growth Data and NSF Irradiation Growth Data

Figure Note: GNF channel growth data and NSF irradiation growth data collected at BOR-60 plotted relative to open literature data for Zircaloy-2. The fluence of the data collected at BOR-60 (Reference 18) and in a PWR (Reference 42) has been corrected for the BWR neutron energy distribution at 40% void (See Reference 43).

[[

]]
]]

Figure 2-14 Irradiation Growth Data on a Series of Zr-Nb-Sn-Fe Alloys

Figure Note: Irradiation growth data on a series of Zr-Nb-Sn-Fe alloys that were irradiated at BOR-60 and reported in Reference 18. The BOR-60 fluences have been corrected to be equivalent to the BWR neutron energy distribution at a 40% void fraction (See Reference 43).

[[

]]

]]

Figure 2-15 Irradiation Growth Data on a Series of Zr-1Nb-1Sn Alloys

Figure Note: Irradiation growth data on a series of Zr-1Nb-1Sn alloys with varying amounts of Fe that were irradiated at BOR-60 and reported in Reference 18. The BOR-60 fluences have been corrected to be equivalent to the BWR neutron energy distribution at a 40% void fraction (See Reference 43).

[[

]]

Figure 2-16 Fatigue Data for Zircaloy Used in Fatigue Evaluations for Cladding (References 26, 37, and 38)

[[

]]

Figure 2-17 NSF and Zircaloy-2 Fatigue Data

Figure Note: NSF and Zircaloy-2 fatigue data generated with an hourglass shaped fatigue sample plotted relative to the NRC accepted mean and upper/lower 95/95 boundaries for Zircaloy cladding (Reference 26).

[[

]]

Figure 2-18 Comparison of Zircaloy-2 and NSF Tested Using Similar Applied Stresses

Figure Note: Comparison of Zircaloy-2 and NSF tested using similar applied stresses at 752°F (400°C) compared to the stress rupture predictive equation.

[[

]]

Figure 2-19 Comparison of Irradiated Zircaloy-2 Tested at 550°F(288°C) and Irradiated NSF Tested at 752°F(400°C)

Figure Note: Comparison of irradiated Zircaloy-2 tested at 550°F (288°C) and irradiated NSF tested at 752°F (400°C) relative to their respective predictive equation for stress rupture.

[[

]]

Figure 2-20 Measured Hydrogen Pickup in a NSF Channel

Figure Note: Measured hydrogen pickup in a NSF channel compared to a Zircaloy-2 channel operated in symmetric locations. The mass basis for normalizing the calculated hydrogen generated in wppm is the metal. [[

]]

[[

]]

Figure 2-21 Photomicrograph of Precipitated Hydrides

Figure Note: Photomicrograph of precipitated hydrides oriented perpendicular to the through thickness direction in a NSF channel component (152 wppm H).

3.0 CALCULATING CPR WITH NSF CHANNELS

3.1.1 GNF Methodology for Critical Power Ratio Calculations

This section describes the current method for calculating CPR, specifically highlighting the dependence of R-factor on channel bow. This section is provided for informational purposes only and is intended to provide clarification on the method for establishing dependence of bundle R-factors and CPRs on channel bow as documented in Reference 44.

3.1.2 Critical Power Ratio and R-Factor Methodology

The method for calculating CPR and bundle R-factors is described in NEDC-32505P Revision 1 (Reference 45) for GE11, GE12, and GE13. This method is identical to that described in NEDC-33292P Revision 3 (Reference 46) for GNF2 fuel and NEDC-32851P Revision 5 for GE14 fuel (Reference 47). In these documents, it is stated that the effects of channel bow are accounted for on an individual fuel rod power basis.

3.1.3 R-Factor Calculational Process

As described in Reference 45, the steps used in the R-factor calculational process are as follows:

1. Obtain relative 2D rod-by-rod power distributions from the lattice physics code. These values are a function of lattice nuclear design, average exposure, void fraction and control state.
2. [[

]]
3. Calculate an R-factor for each individual fuel rod. [[

]]
4. The bundle R-factor is the maximum value from all individual rod R-factors.
5. Repeat these calculations for each desired bundle average exposure, control fraction and channel bow.

[[

]]

As demonstrated in this clarification, the amount of channel bow serves only as an input to these calculations; therefore, implementation of NSF will have no effect on the process to calculate either CPR or bundle R-factors. No change to process related to either CPR or R-factor calculations is intended or required based on this LTR approval. The only change being recommended [[ ]]

3.1.4 Current Procedure for Assigning Bow-Specific R-factors

[[

]]

The shadow-corrosion bow phenomenon was not recognized until after the development of the current process. However, because shadow-corrosion bow results in the channel bowing back towards the control blade, it generally reduces the total amount of bow, which on average is away from the blade. In extreme cases, shadow-corrosion bow can result in the water gap decreasing on the blade side of individual bundles and increasing on the opposite side. [[

]]

3.1.5 Bow-Specific R-Factor Calculations Procedure for NSF Channels

As described above, the current procedure for determining BOWAVE considers effects of initial as-manufactured channel bow and fluence-induced bow. [[

]] For clarity, the variable CACABO will be used to represent the core-average, cell-average bow as calculated by the 3-D core simulator. [[

]] The models for calculating channel bow and CACABO that are used in the 3-D core simulator are provided for information in Appendix A.

[[

]] versus using the calculated value of CACABO from the 3D core simulator has been quantified. The absolute difference in the Maximum Fraction of Limiting CPR (MFLCPR) for a given plant cycle as a function of exposure is used to demonstrate this effect. Figure 3-2 illustrates this difference for [[ ]]

[[

]]

The CACABO uncertainty component that feeds into the safety limit minimum CPR (SLMCPR) is plotted in Figure 3-3 versus cycle exposure for [[ ]]. This has been determined using the method described in Appendix A. As seen from the figure, the uncertainty is well below [[ ]]. A [[ ]] is used for the roll-up of the bow uncertainty in the SLMCPR calculations (References 44 and A-2). This [[ ]] will continue to be used as [[ ]]for NSF channels for the roll-up of the uncertainty in the SLMCPR calculations. No credit is taken for the [[ ]] observed in the figure for the NSF channels.

3.2 NSF APPLICATION TO LHGR CALCULATION

[[

]]

[[

]]

Figure 3-1 Calculated Values of CACABO for NSF Cores

[[

]]

Figure 3-2 Absolute MFLCPR Difference

Figure Note: [[

]]

[[

]]

Figure 3-3 Uncertainty in the Core-Average, Cell-Average Bow as a Function of Cycle Exposure

4.0 APPLICABILITY

Upon approval of this licensing topical report, NSF may be incorporated into GNF fuel designs in channels by inclusion in the GESTAR new fuel compliance reports for a specific fuel design, as supported by appropriate analysis using the properties described herein.

As outlined in this LTR, NSF channels have channel bow performance characteristics that are distinctly different than those observed for Zircaloy channels used in CPR evaluations. It is therefore inappropriate to continue using only the Zircaloy-specific, [[

]]

5.0 SUMMARY

This licensing topical report documents the material properties of NSF for application in channels as part of GNF fuel designs. These properties are used in evaluating the adequacy of components designed with NSF. [[

]]

In addition, this licensing topical report documents recommendations related to the bow assessment and application approach in the CPR calculation for NSF channels.

6.0 REFERENCES

1. General Electric Company, "BWR Fuel Channel Mechanical Design and Deflection," NEDE-21354-P, September 1976.

2. General Electric Company, "BWR Fuel Assembly Evaluation of Combined Safe Shutdown (SSE) and Loss-of-Coolant Accident (LOCA) Loadings (Amendment 3)," NEDE-21175-3-P-A, October 1984.

3. McGraw-Hill, "Metallurgy of Zirconium," Lustman, B. and Kerze, F., 1955.

4. Proceedings of the 1st International Conference on the Peaceful Uses of Atomic Energy, "Aqueous Corrosion of Zirconium and Its Alloys at Elevated Temperatures," Volume 9, United Nations, New York, and IAEA, Vienna, Thomas, D.E., p.407, 1956.

5. Proceedings of the 2nd U.N. International Conference on Peaceful Uses of Atomic Energy, "Mechanical Properties and Corrosion Resistance of Zirconium and its Alloys in Water, Steam and Gases at Elevated Temperature," Volume 5, Geneva, CH, Ambartsumyan, R.S. et al., P/2044, 1958.

6. Proceedings of the 2nd U.N. International Conference on Peaceful Uses of Atomic Energy, "Structure and Properties of Zirconium Alloys," Volume 5, Geneva, CH, Ivanov, O.S. and Grigorovich, V.K., P/2046, 1958.

7. UKAEA Harwell, "The Oxidation and Corrosion of Zirconium and Its Alloys: XV Further Studies of Zirconium-Niobium Alloys," Report AERE-R 4134, Cox, B., 1962.

8. Atomic Energy of Canada, Ltd., "Corrosion and Hydriding Behaviour of Some Zr 2.5wt% Nb Alloys in Water, Steam and Various Gases at High Temperature," Chalk River, Dalgaard, S.B., AECL-1513, 1962.

9. Westinghouse Electric Corp., Bettis Atomic Power Laboratory, "The Corrosion and Hydrogen Absorption Properties of Zircaloy-4 Alloys Containing Additions of Niobium," WAPD-TM-647, Kass, S., 1967.

10. Proceedings of the 4th UN International Conference on Peaceful Uses of Atomic Energy, "Corrosion Behavior of Zirconium Alloys in Boiling Water Under Irradiation,"

Volume 10, United Nations, New York, and IAEA, Vienna, Amaev, A.D., et al., p. 537, 1972.

11. Nuclear Science and Engineering, "The Effect of Niobium Additions on the Corrosion Behavior of Zircaloy-4," Volume 63, Sabol, G.P. and McDonald, G.G., p. 83, 1977.

12. 10th International Symposium Symposium on Zirconium in the Nuclear Industry, "In-Reactor Corrosion Performance of ZIRLO™ and Zircaloy-4," ASTM STP 1245, Sabol, G.P., et al., p. 724, 1994.

13. Proceedings, ANS International Topical Meeting on Light Water Reactor Fuel Performance, "In-Reactor Fuel Cladding Corrosion Performance at Higher Burnups and Higher Coolant Temperatures," Portland, OR, Sabol, G.P., et al., p. 397, 1997.

14. 14th International Symposium on Zirconium in the Nuclear Industry, "ZIRLO™ – An Alloy Development Success," ASTM STP 1467, Sabol, G.P., p. 3, 2005.

15. 11th International Symposium on Zirconium in the Nuclear Industry, "Zirconium Alloy E635 as a Material for Fuel Rod Cladding and Other Components of VVER and RBMK Reactors," ASTM STP 1295, Nikulina, A.V., et al., p. 785, 1996.

16. Moscow Engineering Physics Institute, "Fundamental Research of Materials Structure and Properties Changed Resulted from Irradiation by Means of Complex of Modern Physical Methods," ISTC Project #597, October 2006.

17. 15th International Symposium on Zirconium in the Nuclear Industry, et al., "Irradiation-Induced Growth and Microstructure of Recrystallized, Cold Worked and Quenched Zircaloy-2, NSF, and E635 Alloys," ASTM STP 1505, Kobylyansky, G. P., p. 564, 2009.

18. EPRI, "The NFIR-V Dimensional Stability Project: BOR-60 Irradiation and Growth Data," EPRI Report 1021035, June 2010.

19. Computer Coupling of Phase Diagrams and Thermochemistry, "The Zr-Sn Binary System: New Experimental Results and Thermodymic Assessment," Volume 32, Perez, R.J. et al., pp. 593-601 (2008).

20. International Atomic Energy Agency, "The Metallurgy of Zirconium," Vienna, Douglass, D.L., 1971.

21. Journal of Nuclear Materials, "Effect of β Phase, Precipitate and Nb-Concentration in Matrix on Corrosion and Oxide Characteristics of Zr-xNb Alloys," Volume 317, Jeong, Y.H., et al., pp.1-12, 2003.

22. 14th International Symposium on Zirconium in the Nuclear Industry, "Influence of Structure – Phase State of Nb containing Zr Alloys on Irradiation-Induced Growth," ASTM STP 1467, Shishov, V.N. et al., p. 666, 2005.

23. 11th International Symposium on Zirconium in the Nuclear Industry, "Influence of Processing Variables and Alloy Chemistry on the Corrosion Behavior of ZIRLO Nuclear Fuel Cladding," ASTM STP 1295, Comstock, R.J., Schoenberger, G. and Sabol, G.P., p. 710, 1996.

24. 13th International Symposium on Zirconium in the Nuclear Industry, "Alternative Zr Alloys with Irradiation Resistant Precipitates for High Burnup BWR Applications," ASTM STP 1423, Garzarolli, F., et al., p. 119, 2002.

25. Pergamon Press, "Engineering Materials 1: An Introduction to their Properties and Applications," Chapter 6, Ashby and Jones, 1980.

26. Global Nuclear Fuel, "Licensing Topical Report: The Prime Model for Analysis of Fuel Rod Thermal – Mechanical Performance; Part 1 – Technical Bases," NEDE-33256P-A, Revision 2, September 2010.

27. Hemisphere Publishing Corporation, "Introduction to Metallurgical Thermodynamics," 2nd Edition, Gaskell, D.R., pp. 114-122, 1981.

28. John Wiley and Sons Inc., "Thermodynamics of Solids," Second Edition, Swalin, R.A., p. 83, 1972.

29. John Wiley and Sons, Inc. "Materials Science and Engineering: An Introduction," 4th Edition, Callister, W.D., pp. 657, (1997).

30. Knolls Atomic Power Laboratory, "Application of the Ewing Equation for Calculating Thermal Conductivity from Electrical Conductivity," KAPL-2146, April 7, 1961.

31. Franklin, D.G., Lucas, G.E., and Bement, A.L., "Creep of Zirconium Alloys in Nuclear Reactors," STP 815, ASTM (1983).

32. Nuclear Engineering and Design, "Transitions in Creep Mechanisms and Creep Anisotropy in Zr-1Nb-1Sn-0.2Fe Sheet," Volume 156, Murty, K.L. et al., p. 359, 1995.

33. Journal of Nuclear Materials, "Irradiation-Induced Microstructural Changes in Zr – 1% Sn – 1% nb – 0.4% Fe," Volume 238, Nikulina, A.V. et al., p 205, 1996.

34. 6th International Symposium on Zirconium in the Nuclear Industry, "Irradiation Growth of Zircaloy (LWBR Development Program)," ASTM STP 824, Willard, H.J., p. 452, 1984.

35. 15th International Symposium on Zirconium in the Nuclear Industry, "In-Reactor Deformation of Zirconium Alloy Components," ASTM STP 1505, Holt, R.A., p. 3, 2009.

36. EPRI, "The NFIR-V Dimensional Stability Project: Post-Irradiation Examination Results on Material Variants Irradiated in BOR-60," EPRI Report 1022905, December 2011.

37. Nuclear Science and Engineering, "Fatigue Design Basis for Zircaloy Components," Volume 20, O'Donnell, W.J. and Langer, B.F., p.1, 1964.

38. Journal of Nuclear Materials, "Low Cycle Fatigue Properties of Zircaloy Cladding," Volume 56, Pettersson, K., pp. 91-102, 1975.

39. Metallurgical Transaction. A, "The Influence of Multiaxial States of Stress on the Hydrogen Embrittlement of Zirconium Alloy Sheet," Volume 16A, F. Yunchang and D. Koss, p. 675 (1985).

40. Nuclear Engineering and Design, "Analysis of the Fracture Behavior of Hydrided Fuel Cladding by Fracture Mechanics," Volume 203, M. Kuroda, et al. p. 185, (2001).

41. CRC Press, "CRC Handbook of Chemistry and Physics," 71st Edition, pp. 5-68 – 5-69, (1990 – 1991).

42. Zirconium in the Nuclear Industry: Twelfth International Symposium, "Post-Irradiation Characterization of Ultra-High-Fluence Zircaloy-2 Plate," ASTM STP1354, Mahmood, S. et al. p. 139, 1998.

43. EPRI, "NFIR Dimensional Stability Project: A Method for Transposing Test Reactor Irradiation Data for PWR and BWR Applications," EPRI Report 1019098, October 2009.

44. Letter and attachments to Robert C. Jones, Chief Reactor Systems Branch - USNRC, ''Fuel Channel Bow Assessment," November 15, 1989, JSC89115, MFN086-89.

45. GE Nuclear Energy, "R-Factor Calculation Method for GE11, GE12 and GE13 Fuel," NEDC-32505P-A, Revision 1, July 1999.

46. Global Nuclear Fuel, "GEXL17 Correlation for GNF2 Fuel," NEDC-33292P, Revision 3, April 2009.

47. Global Nuclear Fuel,"GEXL14 Correlation for GE14 Fuel," NEDC-32851P-A, Revision 5, April 2011.

48. Global Nuclear Fuel, "The PRIME Model for Analysis of Fuel Rod Thermal – Mechanical Performance Part 3 – Application Methodology Licensing Topical Report," NEDC-33258P-A, Revision 1, September 2010.

49. Global Nuclear Fuel, "Applicability of GE Methods to Expanded Operating Domains Licensing Topical Report," NEDC-33173P-A, Revision 1, September 2010.

APPENDIX A
CALCULATING CORE-AVERAGE, CELL-AVERAGE BOW FOR NSF CHANNELS

A.1 CORE-AVERAGE CELL-AVERAGE BOW (CACABO)

This appendix describes the methodology utilized to calculate CACABO for a plant cycle and presents models validating the approach. The sections are divided as described below:

1. Section A.2 – Description and validation of channel bow calculation methodology on an individual bundle basis for NSF, including,
    a. Initial manufactured channel bow, described in Section A.2.1
    b. Fluence-induced bow, described in Section A.2.2
    c. Shadow-corrosion induced bow, described in Section A.2.3
    d. Qualification of the individual channel bow models for NSF, Section A.2.4
2. Section A.3 - Description of cell-average bow calculation methodology,
3. Section A.4 - Description of core-average, cell-average bow calculation methodology.

A.2 INDIVIDUAL CHANNEL BOW CALCULATION APPROACH

The total bow of an individual channel results from the cumulative effect of the initial manufactured bow, fluence induced bow, and shadow bow.

A.2.1 INITIAL MANUFACTURED CHANNEL BOW

During the manufacturing process, some nominal amount of channel bow is inherently introduced into the finished product. For this reason, channels with no irradiation history (beginning of life channels) still are characterized by some amount of channel bow. [[

]]

A.2.2 FLUENCE-INDUCED BOW CALCULATION

Fast fluence (E>1MeV) gradient induced bow results from differential growth of channel material on opposite channel faces. The growth is towards the longer side to maintain a minimal stress condition. The steps to calculate fluence-induced bow of a channel can be summarized as follows:

1. Define the accumulated channel wall fluence, as described in Section A.2.2.1,
2. Calculate the irradiation growth strain of the channel wall segments due to the presence of fast fluence, as described in Section A.2.2.2. The growth strain is given in a dimensionless form (in/in), where the denominator is the length over which the strain is applicable.
3. With the growth strain known over a given length (segment) and for all sides of the channel, it is then possible to calculate the fluence-induced bow of this channel, as described in Section A.2.2.3.

A.2.2.1 ACCUMULATION OF CHANNEL FLUENCE

GNF lattice-physics codes calculate the fraction of fast flux (flux above 1MeV) as a function of void and exposure for each lattice in the core. GNF core simulators take these values and calculate the channel surface-center flux above 1MeV on a channel surface, node specific basis. When performing this assessment, the channel numbering (n=1,..,4) is with respect to control blade position, as shown in Figure A-1.

Using this numbering scheme, the channel surface, node specific flux (FLUXS(k,i,j,n)) is tracked as a function of the node center fast flux, node width, water gap size, diffusion coefficients, and discontinuity factors. These channel surface fluxes are used to track channel surface fluence over a cycle on a nodal basis as follows:

$$\boldsymbol{FLUNCE(k,i,j,n) = FLUNCE_{t-1}(k,i,j,n) + DT * FLUXS(k,i,j,n)} \quad \textbf{(A-1)}$$

where:

$FLUNCE(k,i,j,n)$	Is the surface-center fluence (n/cm^2)
$FLUNCE_{t-1}(k,i,j,n)$	Is the surface-center fluence from prior exposure step (n/cm^2)
DT	Is the time in seconds consistent with the exposure increment
$FLUXS$(k,i,j,n)	Is the channel surface, node specific flux (n/cm^2-s)

A.2.2.2 IRRADIATION GROWTH STRAIN

Irradiation growth strain is defined as a function of channel fluence. It is expressed as ε_n for face *n* in the following section when describing the channel bow calculation process.

A.2.2.3 EVALUATION OF FLUENCE CHANNEL BOW

The evaluation of the bow of a single channel is performed in a step-wise fashion for each channel surface pair (n=(1,3) and n=(2,4)), as outlined below:

1. [[

]]

A.2.2.4 CALCULATION OF DEFLECTION OF A CHANNEL SEGMENT

For a single segment, as shown in Figure A-3, the amount of fluence induced channel bow can be defined as by Equation (A-4).

[[

]]

A.2.2.5 CALCULATION OF CHANNEL BOW AS A FUNCTION OF AXIAL HEIGHT

The fluence induced bow of a channel at a given axial height is a function [[

]]

A.2.3 SHADOW-CORROSION INDUCED BOW CALCULATION

Shadow corrosion is an enhanced irradiation corrosion mechanism that occurs on zirconium alloys when a dissimilar material (such as a control blade) is near the zirconium surface (such as a BWR channel) and the water chemistry is oxygenated. When a fuel bundle is controlled early in life, the increased corrosion on the blade side relative to the non-blade side results in a

difference in hydrogen absorbed in channel material. Hydrogen is absorbed into the metal as part of the corrosion process and causes a volume change resulting in channel bow.

Because direct measurement of shadow corrosion-induced bow is only possible when the fluence gradient is zero, shadow bow is generally observed by accounting for the fluence gradient induced bow. After accounting for fluence bow in the data, the end-of-life channel bow correlates well with the total effective control blade exposure (ECBE).

Prediction of shadow bow involves two parts. The first part is calculation of ECBE for each channel (this is a measure of the susceptibility to shadow-corrosion induced bow). The second part is using an empirical correlation to convert the ECBE to a corresponding shadow-induced bow. Both parts are described in more detail in the following sections.

A.2.3.1 ACCUMULATION OF CONTROLLED TIME

ECBE is the summation of insertion length in inches times the length of control period in days, weighted by a weight factor, as described in the equation below.

[[

]]

A.2.3.2 EVALUATION OF SHADOW CORROSION-INDUCED BOW

[[

]]

[[

]]

A.2.4 QUALIFICATION OF FLUENCE AND SHADOW BOW MODELS FOR NSF

The purpose of this section is to provide the evidence necessary to qualify the channel bow models that will be used in calculating the core-average, cell-average bow, which is an input to calculate the CPR. [[

]] The relative range of exposures and ECBE are provided in Figure A-5. The NSF channel data reasonably represents the operating conditions experienced by channels over their lifetimes.

The evaluation of the channel bow data is complex because two independent mechanisms cause bow. The evaluation approach taken is to first qualify the predicted bow when only fluence gradient-induced bow is active [[ ]]and then evaluate shadow corrosion-induced bow as a function of ECBE after subtracting the effect of fluence gradient-induced bow.

The measured bow is plotted versus the predicted fluence gradient-induced bow (Figure A-6) using the model described in Section A.2.2. The line through the data represents the one-to-one relationship between measured and predicted bow. [[

]]

When the shadow corrosion-induced bow mechanism was being recognized, one of the most important observations was that there was a positive bias in the residuals of the fluence gradient-

induced bow predictions when channels experienced early-life control (Reference A-1). [[

]] This bias in the residual is now considered the inferred shadow bow and is found to be correlated to ECBE (Figure A-9). The model described in Section A.2.3 is also provided for comparison to the data.

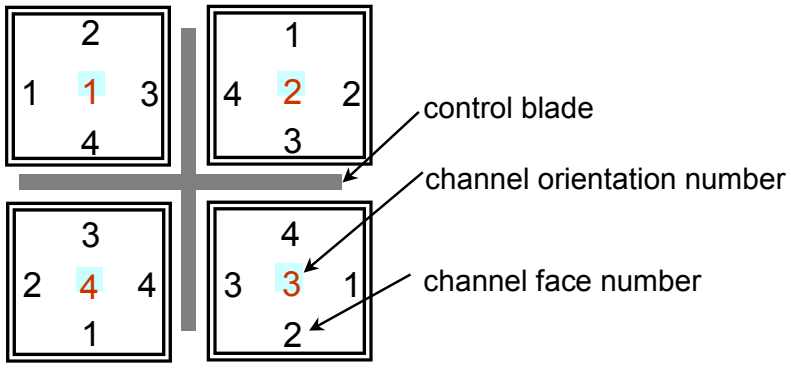

Figure A-1 Channel Face Numbering for the Bow Model

[[

]]

Figure A-2 Calculation of Segment Edge Bow

[[

]]

Figure A-3 Fluence Induced Bow

[[

]]

Figure A-4 Channel Bow Calculation

[[

]]

Figure A-5 Range of ECBE and Exposure in the Channel Distortion Database for NSF Channels

[[

]]

Figure A-6 Measured Bow Plotted as a Function of Predicted Fluence Bow for NSF Channels

[[

]]

Figure A-7 Residual (Measured – Predicted) of Fluence Gradient-Induced Bow Data

Figure Note: Residual (measured – predicted) of fluence gradient-induced bow data **[[** **]]** for the NSF channel database.

[[

]]

Figure A-8 Residual (Measured – Predicted Fluence Bow) of Fluence Gradient-Induced Bow Data

Figure Note: Residual (measured – predicted fluence bow) of fluence gradient-induced bow data **[[ ]]**and data susceptible to shadow corrosion-induced bow **[[ ]]** for the NSF channel database. The data available for NSF [[ ]].

[[

]]

Figure A-9 Inferred Shadow Bow (Measured – Predicted Fluence Bow) as a Function of ECBE for the NSF Database

Figure Note: Only data from channels with exposures greater than **[[** **]]** are included because this represents the exposure where shadow bow has fully accumulated.

A.3 CELL-AVERAGE BOW CALCULATION

The mean bow based on manufacturing, fluence, and shadow corrosion for a given channel at core position (i,j) is obtained using the following formulas:

[[

]]

This method changes the cell-average bow by including a [[

]]

A.4 CORE-AVERAGE CELL-AVERAGE BOW AND UNCERTAINTY CALCULATION

The cell-average bows are combined to determine the core-average, cell-average bow (CACABO) and the uncertainty as shown in Equations (A-23) and (A-24). [[

]]

A.5 REFERENCES

A-1 16th International Symposium on Zirconium in the Nuclear Industry, "Shadow Corrosion-Induced Bow of Zircaloy-2 Channels," ASTM STP 1529, Mahmood, S.T., et al., p. 954, 2011.

A-2 GE Nuclear Energy, "Methodology and Uncertainties for Safety Limit MCPR Evaluations," NEDC-32601-P-A, August 1999.